Check for updates

Carbon-wrapped Fe–Ni bimetallic nanoparticle-catalyzed Friedel–Crafts acylation for green synthesis of aromatic ketones†

Hao Zhang, [iD] ‡[a] Xiaojing Song,‡[b] Hao Sun,[c] Zhenyu Lei,[a] Shouxin Bao,[d] Chen Zhao,[a] Dianwen Hu,[a] Wenxiang Zhang,[a] Jingyao Liu [iD] *[c] and Mingjun Jia [iD] *[a]

Developing highly efficient and durable eco-friendly heterogeneous catalysts for the Friedel–Crafts acylation (FCA) reaction has been a long-term and significant target, yet remains a great challenge. Herein, a series of Fe–Ni alloy nanoparticles (NPs) encapsulated inside N-doped carbon spheres (Fe_xNi_{1-x}@NC) was rationally fabricated by pyrolyzing the Fe–Ni bimetallic metal–organic frameworks (BMOFs-Fe_xNi_{1-x}) to this end. Various characterization results demonstrated that FeNi alloy NPs (25 nm) covered by a thin carbon shell (5 nm) were uniformly distributed throughout the entire carbon-based composite. A number of oxidized metal species (Fe^{3+}, Ni^{2+}) are present on the surface of the inner bimetallic core, which should be the main source of catalytically active centers of the carbon-wrapped metal NP catalysts. The composition-optimized $Fe_{0.8}Ni_{0.2}$@NC with relatively higher positive surface charges exhibited the highest catalytic activity and excellent stability for the acylation of aromatic compounds with acyl chlorides. The density functional theory calculations revealed that the catalytic activity of the Fe_xNi_{1-x}@NC catalysts could arise from the electron transfer, *i.e.*, from the outermost layer of the carbon shell to the inner positively charged Fe-based metal NPs, which can lead to a positive charge distribution (by acting as weak Lewis acid sites) on the external surface of the carbon-encapsulated metal NP catalysts. In this case, the external carbon shell can function as 'chainmail' to transfer the Lewis acidity (positive charge), and also to protect the inner metal core from the destructive reaction environment, thus resulting in the formation of highly efficient and durable FCA catalysts.

1. Introduction

Developing eco-friendly efficient heterogeneous catalysts for Friedel–Crafts acylation (FCA) reactions is a very attractive research subject because it may offer an environmentally friendly way to produce aromatic ketone compounds.[1] A variety of solid acid catalysts, including supported heteropolyacids, metal oxides, metal–organic frameworks (MOFs), and zeolites, have shown relatively high catalytic activity for various FCA reactions, demonstrating the great potential for replacing the traditional homogeneous Lewis acid catalysts (*e.g.*, $AlCl_3$ and $FeCl_3$).[2–8] However, these solid acid catalysts commonly undergo easy leaching of the active species or rapid deactivation during the reaction term, which are caused by the strong dissolving and complexing capability of the generated HCl and aromatic ketone.[3,8] Hence, considerable effort is still required to design more stable and green solid acid catalysts for FCA reactions.

Recently, high-temperature pyrolysis of MOFs has shown great advantages in creating functional composite materials with abundant porosity, and excellent chemical and mechanical stabilities.[9–11] In particular, some Fe-containing MOFs have been used as versatile precursors to prepare stable porous carbon-supported Fe-based composites with superior catalytic activity and stability for some important catalytic processes.[12–14] For instance, Xu's group reported that atomic Fe/N doping in hierarchical graphitic carbon, derived from $Fe-MIL-101-NH_2$, could be widely used as an extremely efficient electrocatalyst.[15] Tang and coworkers developed carbonized Fe-based NPs *via* the pyrolysis of monodispersed nanoscale $MIL-88B-NH_3$, which could act as highly active electrocatalysts for oxygen reduction reactions.[16]

[a] *Institute of Physical ChemistryCollege of Chemistry, Jilin University, Changchun 130012, Jilin, China. E-mail: jiamj@jlu.edu.cn*

[b] *State Key Laboratory of Catalysis, iChEM, Dalian Institute of Chemical Physics, Chinese Academy of Sciences, Dalian 116023, Liaoning, China*

[c] *Laboratory of Theoretical and Computational Chemistry, Institute of Theoretical Chemistry, Jilin University, Changchun 130012, Jilin, China. E-mail: ljy121@jlu.edu.cn*

[d] *State Key Laboratory of Inorganic Synthesis and Preparative Chemistry, College of Chemistry, Jilin University, Changchun 130012, Jilin, China*

† Electronic supplementary information (ESI) available: Detailed experimental data and characterization results. See DOI: 10.1039/d1cy01304a

‡ These authors contributed equally to this work.

This journal is © The Royal Society of Chemistry 2021

Catal. Sci. Technol., 2021, 11, 7943–7954 | 7943

It was also reported that the catalytic performance of the Fe-containing porous carbon composites might be further enhanced by introducing a second metal element into the precursor of Fe-MOFs.[17–23] For example, Thomas et al. used a bimetallic MIL-88-Fe/Ni-dicyandiamide composite as the precursor to synthesize a carbon-based FeNi alloy catalyst with increased activity and stability for electrocatalysis.[24] It was proposed that the Ni additive in these composite catalysts could act as a structural promoter to disperse and stabilize the Fe species, and might also assume a synergistic role to further enhance the catalytic performance of the composite catalysts.[25–30]

Inspired by these advances in preparing functional Fe-containing carbon-based catalysts through the pyrolysis route, we recently tried to develop a graphitic carbon-encapsulated iron carbide catalyst by pyrolyzing Fe-diamine-dicarboxylic acid MOFs at high temperature.[31,32] The resultant Fe-based catalysts exhibited high catalytic activity for the FCA reactions with acyl chloride as the acylation agent. More significantly, the condition-optimized catalyst, termed as Fe@NC-800, showed excellent stability and could easily be recycled after simple filtration.[31]

Recently, we found that $Fe_xC/NC-0.05$, derived from the pyrolysis of bimetallic metal organic frameworks (BMOFs)-$ZnFe_{0.05}$, exhibited catalytic activity more enhanced than that of Fe@NC-800.[32] Although the Zn species in the BMOF precursors could be nearly completely removed during the pyrolysis process, it is likely that the evaporation of Zn under high temperature would efficiently preclude the agglomeration of the Fe-based NPs, and enlarge the specific surface of the resultant pyrolyzed carbon-based materials.[33–36]

Despite this progress, further work is required to enhance the catalytic efficiency of the carbon-wrapped Fe-based NPs, and to obtain answers for some basic questions,[37–39] such as: what are the main active sites of the carbon-wrapped Fe-based NP catalyst in the FCA reactions, and how could the resultant active centers survive under the harsh environment, i.e., surrounded by in situ-formed products of HCl and aromatic ketone?

Herein, we report the preparation of a family of FeNi bimetallic alloy NPs encapsulated in carbon networks (Fe_xNi_{1-x}@NC) by pyrolyzing the precursors of bimetallic MOFs (BMOFs-Fe_xNi_{1-x}), and their catalytic properties were investigated for the FCA reactions of aromatic compounds with acyl chloride. A variety of characterization results demonstrated that a greater number of catalytically active sites may be produced after the addition of a suitable amount of metal Ni into the Fe-based carbon catalysts, resulting in an increase of the catalytic efficiency for FCA reactions.

The density functional theory (DFT) calculations reveal that a partial electron transfer may occur from the outermost layer to the inner FeNi NPs induced by the positive Fe^{3+} (or Ni^{2+}) cations distributed on the inner surface of the metal core, which can lead to a positive charge distribution on the external surface of carbon-encapsulated FeNi NP catalysts. In this case, the concept of 'chainmail catalyst' proposed by Deng and co-workers could be used to describe the main features of the carbon-wrapped Fe-based catalysts,[40,41] and thus may provide a relatively reasonable explanation regarding why this type of catalyst possesses high activity and structural stability under the harsh reaction environment.

2. Experimental

2.1 Materials

Terephthalic acid, 1,4-diazabicyclo[2.2.2]octane, $NiCl_2·6H_2O$, and $FeCl_2·4H_2O$ were purchased from Tianjin Guangfu Fine Chemical Research Institute. Aromatic compounds such as m-xylene and corresponding aromatic ketones as well as acylation agents such as benzoyl chloride were obtained from Tokyo Chemical Industry (TCI) in Shanghai. N,N-Dimethylformamide (DMF), ethanol, dodecane, and other solvents were purchased from Aladdin. All reagents were of analytical grade and were used without further purification.

2.2 Synthesis of BMOFs-Fe_xNi_{1-x}

The Fe–Ni bimetallic MOFs (BMOFs-Fe_xNi_{1-x}) were solvothermally synthesized according to previously published procedures.[42,43] In a typical synthetic process, terephthalic acid (TPA, 3.0 mmol) and 1,4-diazabicyclo[2.2.2]octane (DABCO, 3.0 mmol) were mixed with N,N-dimethylformamide (DMF, 60 mL) in a 100 mL Teflon-lined stainless steel autoclave under stirring. After that, a mixture of $FeCl_2·4H_2O$ and $NiCl_2·6H_2O$ with different molar ratios of Fe^{2+}/Ni^{2+} was dissolved in the above solution, where the total molar amounts of Fe and Ni were 1.0 mmol, with the stoichiometric number represented by x and $1 - x$ in moles. After continuous stirring for 3 h, the mixture was transferred into an autoclave and heated in an oven at 150 °C for 24 h. After cooling to room temperature, the precipitates were isolated by centrifugation and washed with excess DMF and ethanol to remove the residual organic ligands. Finally, the products of BMOFs-Fe_xNi_{1-x} were collected and dried in air at 80 °C for 24 h, and labelled as BMOFs-Fe, BMOFs-$Fe_{0.9}Ni_{0.1}$, BMOFs-$Fe_{0.8}Ni_{0.2}$, BMOFs-$Fe_{0.5}Ni_{0.5}$, and BMOFs-Ni.

2.3 Synthesis of Fe_xNi_{1-x}@NC

The as-synthesized BMOFs-Fe_xNi_{1-x} was dispersed in a ceramic boat, and then was heated in a furnace protected by flowing nitrogen. The temperature of the furnace was first increased to 200 °C over 1.5 h and further ramped up to 800 °C at 3 °C min^{-1}, and held there for an additional 3 h. The furnace was subsequently turned off and the system allowed to cool. Then, the pyrolysis product of Fe_xNi_{1-x}@NC was obtained in the form of a black powder.

2.4 Characterization

The N_2 adsorption/desorption isotherms were measured with a Micromeritics ASAP 2020 Plus HD88 analyzer at 77 K.

Samples were degassed in a vacuum at 200 °C for 12 h before measurements. The Brunauer–Emmett–Teller (BET) method was used to calculate the specific surface area, and the pore volume was deduced using the adsorbed quantity of nitrogen at $P/P_0 = 0.99$. The pore size distributions were calculated by the Barrett–Joyner–Halenda (BJH) method. The metal contents of catalysts were analyzed by inductively coupled plasma-mass spectrometry (ICP-MS) analysis using an Agilent 725 ICP instrument. The morphologies and structures of the catalysts were characterized with field-emission scanning electron microscopy (FE-SEM, Hitachi SU8020, 3 KV) and transmission electron microscopy (TEM, JEM-1200EX, 200 KV).

High-angle annular dark-field scanning transmission electron microscopy (HAADF-STEM) and energy dispersive X-ray (EDX) elemental mapping measurements were carried out with a JEM-1200EX field-emission transmission electron microscope operating at 200 kV acceleration voltage. The carbon and nitrogen in the samples were measured using a PerkinElmer 2400 CHN elemental analyzer. The crystal structures of all the synthesized BMOFs and related derivative materials were confirmed by powder X-ray diffraction (XRD) using a Shimadzu XRD-6000 diffractometer with filtered Cu Kα radiation. Diffraction patterns were collected at a scan rate of 5° min⁻¹ at 0.02° steps from 10 to 80° two theta. The NETZSCH/STA499 F3/QMS403D/Bruker V70 analyses were used to carry out the thermogravimetry (TG) and thermogravimetry coupled mass spectrometry (TG-MS) characterizations in the temperature range of 40–900 °C at a heating rate of 10 °C min⁻¹ under an Ar flow of 50 mL min⁻¹. The X-ray photoelectron spectroscopy (XPS) analyses were conducted using a VGESCA LAB MK-II X-ray electron spectrometer with Al-Kα radiation.

2.5 Catalytic reaction

A mixture of 50 mg catalyst, m-xylene (2.5 mL, 20 mmol), benzoyl chloride (1.2 mL, 10 mmol), and dodecane (2.3 mL, 10 mmol) as an internal standard was placed in a 10 mL sealed tube under an ambient atmosphere. The reaction was magnetically stirred at 130 °C for several hours. After completion of the reaction, the suspension was filtered, and the filtrate was used for examination of the conversion of benzoyl chloride by a FuLi-9790 II gas chromatograph (GC).

2.6 Recycling procedure

The recyclable catalysts were separated by simple filtration and dried at 80 °C for 12 h. After that, the catalyst was used for further cyclic tests of the FCA reactions. This recycling procedure was repeated more than three times to determine the recyclability of the catalysts.

2.7 DFT computational methods

Spin-polarized density functional theory (DFT) calculations were carried out using the Vienna *ab initio* simulation package (VASP).[44] The projector augmented wave method with a cutoff energy of 400 eV was adopted,[45] and the generalized gradient approximation (GGA) with the Perdew–Burke–Ernzerhof (PBE) functional was used to treat the exchange–correlation energy.[46] The van der Waals interaction was described by the Grimme-D3 semiempirical dispersion correction.[47] To simplify the calculation, the catalyst models were established, consisting of four layers of defective graphene and a C_{78} encapsulating a Fe_{16} cluster coordinated with an O or Cl atom. The first Brillouin zone was sampled by the Monkhorst–Pack method with $1 \times 1 \times 1$ and $3 \times 3 \times 1$ k-point grids for geometry optimization and electronic structure calculations, respectively. The convergence criteria of energy and force were set to 1×10^{-4} eV and 0.05 eV Å⁻¹, respectively.
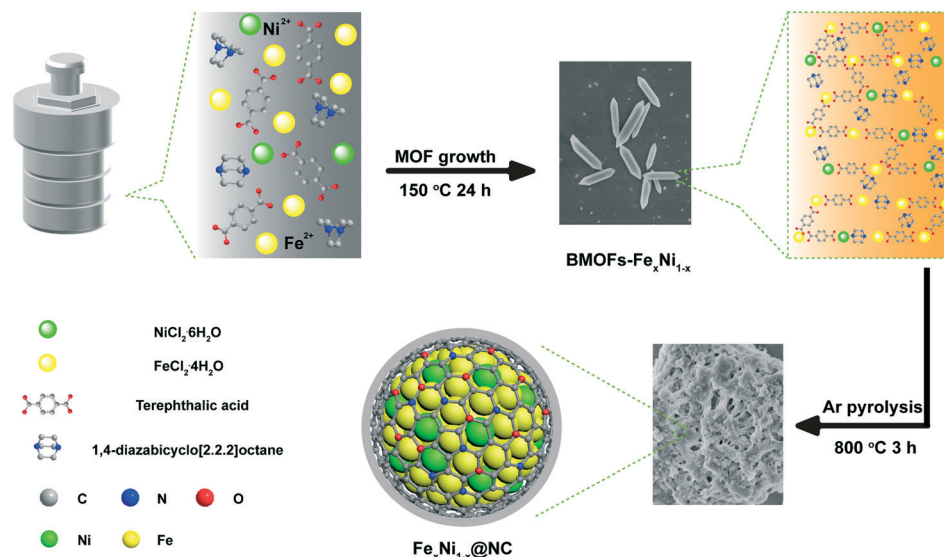
3. Results and discussion

3.1 Material synthesis and characterizations

As shown in Scheme 1, a family of bimetallic MOF (BMOF) precursors were solvothermally synthesized by self-assembly of Fe^{2+}/Ni^{2+} species with TPA and DABCO in the solvent of DMF at 150 °C. Their compositions were systematically varied and labelled as BMOFs-Fe_xNi_{1-x} ($x = 1.0, 0.9, 0.8, 0.5$, and 0, respectively). Their SEM images, shown in Fig. 1, clearly indicate that all the Fe-containing MOFs have a uniform spindle-like morphology with relatively smooth surface, while the BMOF-Ni possesses a cuboid morphology.

The XRD patterns of the resulting BMOFs-Fe_xNi_{1-x} are shown in Fig. 2, where those of BMOFs-Fe and BMOFs-Ni match well with the XRD patterns previously reported.[31,43] Additionally, BMOFs-$Fe_{0.8}Ni_{0.2}$ and BMOFs-$Fe_{0.5}Ni_{0.5}$ exhibit XRD patterns similar to those of BMOFs-Fe and BMOFs-Ni, respectively, indicating the successful synthesis of the Fe–Ni bimetallic MOFs with different Fe/Ni ratios.

The corresponding Fe_xNi_{1-x}@NC composite catalysts were obtained through the pyrolysis of the resulting BMOFs-Fe_xNi_{1-x} at 800 °C under an inert atmosphere. The thermogravimetric profiles reveal that the BMOFs-Fe_xNi_{1-x} precursors with different Fe/Ni ratios exhibit quite similar thermal behavior (Fig. S1a†). The thermal stability of BMOFs-$Fe_{0.8}Ni_{0.2}$ is slightly higher than that of other BMOFs-Fe_xNi_{1-x}, implying the presence of relatively strong coordination interaction with the precursor of BMOFs-$Fe_{0.8}Ni_{0.2}$. The TG-MS characterization of BMOFs-$Fe_{0.8}Ni_{0.2}$ shown in Fig. S1b† demonstrates that a small amount of water and DMF solvent trapped inside the pores are first emitted before the temperature reached 200 °C. In the temperature range of 350 to 550 °C, the amount of CO_2 dramatically increases, while less NO_2 signal is detected, which is a clear indication of the decarboxylation process. When the temperature reached 400 °C, a broad peak with MS signal $m/z = 78$ appeared, corresponding to the cracking residue of the MOFs linkers.[48] The fact that no obvious MS signal appears after 650 °C may suggest that the pyrolysis and carbonization of the BMOFs-Fe_xNi_{1-x} should be nearly completed before 650 °C.

This journal is © The Royal Society of Chemistry 2021

Catal. Sci. Technol., 2021, **11**, 7943–7954 | **7945**

Scheme 1 Schematic illustration of the preparation of BMOFs-Fe$_x$Ni$_{1-x}$ and corresponding Fe$_x$Ni$_{1-x}$@NC composites.

Fig. 3 shows the XRD patterns of the pyrolyzed BMOFs-Fe$_x$Ni$_{1-x}$, in which all the derived Fe$_x$Ni$_{1-x}$@NC samples exhibit a weak peak at approximately 26° indexed to the (002) peak of graphitic carbon, confirming the presence of the graphite phase in the composites. The typical XRD diffraction peaks in the Fe@NC catalyst match well with that of Fe$_3$C (JCPDS # 35-0772), as shown in Fig. S2a.†[31] The characteristic peaks of Ni@NC appear at approximately 44.5°, 51.8°, and 76.4°, corresponding to the metal Ni phase (JCPDS #04-0850, Fig. S2c†).[43] As for the other Fe$_x$Ni$_{1-x}$@NC catalysts, three obvious diffraction peaks at approximately 43.6°, 50.8°, and 74.7° are the (111), (200), and (220) planes of the Fe$_{0.64}$Ni$_{0.36}$ alloy (JCPDS # 47-1405, Fig. S2b†), respectively, indicating the formation of the FeNi alloy phase in these pyrolyzed catalysts.[49] The Fe and Ni in the BMOF precursors and the pyrolyzed catalysts were detected by ICP-AES. As shown in Table 1, the Fe/Ni molar ratios in the pyrolyzed Fe$_x$Ni$_{1-x}$@NC

catalysts are quite consistent with respect to the corresponding BMOFs-Fe$_x$Ni$_{1-x}$, although the weight percent of the metal species considerably increases after the high-temperature pyrolysis. Notably, the catalyst Ni@NC exhibits much higher metal content (66.39 wt%) than other Fe-containing catalysts, which should be an indication that the element Fe is more favorable than Ni for the formation of carbonized composites during the pyrolysis process.

Nitrogen adsorption–desorption isotherms were measured to examine the texture parameters of the pyrolyzed catalysts. As shown in Fig. 4, all the isotherms show a steep increase at low relative pressures with a small hysteresis loop in the P/P_0 range between 0.4–0.6, indicating the existence of a mesoporous structure. The pore size distributions of all catalysts are mainly concentrated at approximately 3.7 nm, as given in Table 2, further confirming the mesoporosity of the pyrolyzed catalysts. Additionally, it can be seen that the BET
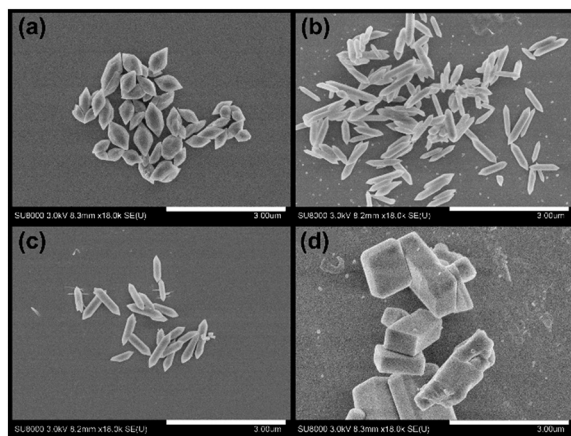

Fig. 1 SEM images of (a) BMOFs-Fe, (b) BMOFs-Fe$_{0.8}$Ni$_{0.2}$, (c) BMOFs-Fe$_{0.5}$Ni$_{0.5}$, and (d) BMOFs-Ni.
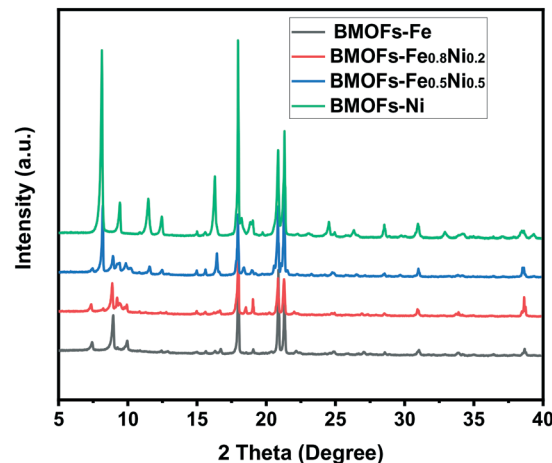

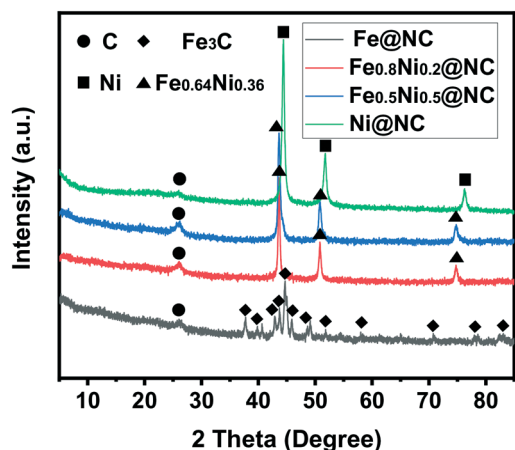**Fig. 2** The XRD patterns of as-synthesized BMOFs-Fe$_x$Ni$_{1-x}$.

7946 | *Catal. Sci. Technol.*, 2021, **11**, 7943–7954

This journal is © The Royal Society of Chemistry 2021

Catalysis Science & Technology

Fig. 3 The XRD patterns of the corresponding Fe_xNi_{1-x}@NC composites.

surface areas of Fe_xNi_{1-x}@NC gradually decrease from 250 m^2 g^{-1} (Fe@NC) to 105 m^2 g^{-1} (Ni@NC) with the increase in Ni content in the precursors of BMOFs-Fe_xNi_{1-x}, suggesting that the addition of Ni is not favorable for the formation of porous carbon.

As shown in Fig. S3,† the SEM images of various Fe-containing catalysts display irregular morphology with a relatively rough surface, while Ni@NC presents in the form of a small cuboid crystal, quite similar to the precursor of BMOFs-Ni. Compared with other samples, $Fe_{0.8}Ni_{0.2}$@NC possesses a larger amount of macropores, implying that the carbonization processes of these materials change somewhat with the change in Fe/Ni ratios in the precursors of BMOFs-Fe_xNi_{1-x}. The TEM images of various Fe_xNi_{1-x}@NC catalysts reveal the presence of a great number of spherical Fe–Ni NPs with an average particle size of approximately 25 nm throughout the carbon matrix (Fig. 5a, S4 and S5†).

HRTEM images of the $Fe_{0.8}Ni_{0.2}$@NC catalyst demonstrate that the spherical FeNi NPs are encapsulated by a few graphitic carbon layers, which affords the evidence of the (111) plane of the $Fe_{0.64}Ni_{0.36}$ alloy phase and the (002) plane of graphite with continuous lattice fringes of 0.21 and 0.34 nm, respectively (Fig. 5c).[49] In addition, the SAED pattern from the red circle region in Fig. 5a exhibits disordered

bright rings, further confirming the coexistence of the FeNi alloy and Fe_3C phases (Fig. 5b).[24] Additionally, the HAADF-STEM image and the corresponding elemental mapping images of $Fe_{0.8}Ni_{0.2}$@NC show that all the elements of C, N, O, Fe, and Ni are uniformly dispersed throughout the carbon matrix.

The XPS spectra of various Fe_xNi_{1-x}@NC catalysts are shown in Fig. 6, S6 and S7.† The survey spectrum in Fig. S6† exhibits intense peaks for Fe, Ni, N, O, and C with bonding energy centered at 710, 853, 400, 530, and 285 eV, respectively, whereas the peaks for Ni 2p in $Fe_{0.9}Ni_{0.1}$@NC and $Fe_{0.8}Ni_{0.2}$@NC are barely discernible (Fig. 6a), indicating the relatively low surface concentration of Ni species (below 0.4 wt%) in these two pyrolyzed catalysts (Table S1†). As for Ni@NC and $Fe_{0.5}Ni_{0.5}$@NC, the spectra of Ni 2p feature two strong signals centered at 870.3 and 853.1 eV accompanied by two satellite peaks, which can be ascribed to the Ni $2p_{1/2}$ and Ni $2p_{3/2}$ in metallic Ni, respectively (Fig. 6a).[30,43] The two distinctive peaks at 855.3 and 872.9 eV are consigned to Ni^{2+} $2p_{3/2}$ and Ni^{2+} $2p_{1/2}$, which were attributed to oxidized nickel species such as NiO and $Ni(OH)_2$.[24,49]

In the Fe 2p XPS spectra of various Fe_xNi_{1-x}@NC catalysts (Fig. 6b), the fitted Fe 2p peaks located at approximately 725.4/711.4 and 720.2/707.3 eV could be assigned to Fe^{3+} and Fe_xC species, respectively.[12,50] Notably, the signals of Fe 2p in $Fe_{0.5}Ni_{0.5}$@NC become very weak, suggesting that the concentration of surface Fe species is rather low due to the introduction of a large amount of Ni in the catalyst. The O 1s peaks of Fe_xNi_{1-x}@NC samples can be fitted by two peaks centered at 530.2 and 532.3 eV, corresponding to the M–O (M = Fe or Ni) and C=O species, respectively (Fig. S7a†).[12] With the increase in the amount of Ni in the Fe_xNi_{1-x}@NC catalysts, relatively high concentrations of C=O species were detected, while the concentration of M–O groups decreased. These results suggest that changing the composition of alloy NPs may influence the distribution and the valence electronic states of metal species (Fe and Ni), implying the existence of relatively strong metal–metal and metal–support interactions.[51–54]

In the C 1s spectra of various Fe_xNi_{1-x}@NC catalysts (Fig. S7b†), the resolved peaks divided into two components centered at 284.8 and 285.9 eV can be attributed to C–C/C=C

Table 1 The element compositions of various samples[a]

Samples	Element analysis						
	C (wt%)	H (wt%)	N (wt%)	O (wt%)	Fe (wt%)	Ni (wt%)	Fe/Ni[b]
BMOFs-Fe	50.32	5.73	7.79	29.81	6.36	0.00	1.00/0.00
BMOFs-$Fe_{0.8}Ni_{0.2}$	50.24	5.21	7.89	29.61	5.55	1.50	0.80/0.20
BMOFs-$Fe_{0.5}Ni_{0.5}$	51.12	5.62	7.96	28.54	3.21	3.55	0.49/0.51
BMOFs-Ni	51.69	5.79	8.35	26.38	0.00	7.79	0.00/1.00
Fe@NC	50.47	0.69	0.82	0.01	48.02	0.00	1.00/0.00
$Fe_{0.8}Ni_{0.2}$@NC	56.02	0.64	0.79	1.12	32.37	9.06	0.79/0.21
$Fe_{0.5}Ni_{0.5}$@NC	55.11	0.50	0.82	1.86	19.73	21.99	0.48/0.52
Ni@NC	32.18	0.45	0.92	0.06	0.00	66.39	0.00/1.00
$Fe_{0.8}Ni_{0.2}$@NC[c]					31.86	8.79	0.79/0.21

[a] Calculated *via* PerkinElmer 2400 CHN elemental analyzer and ICP-AES. [b] Molar ratio of Fe/Ni. [c] Spent catalyst of $Fe_{0.8}Ni_{0.2}$@NC.

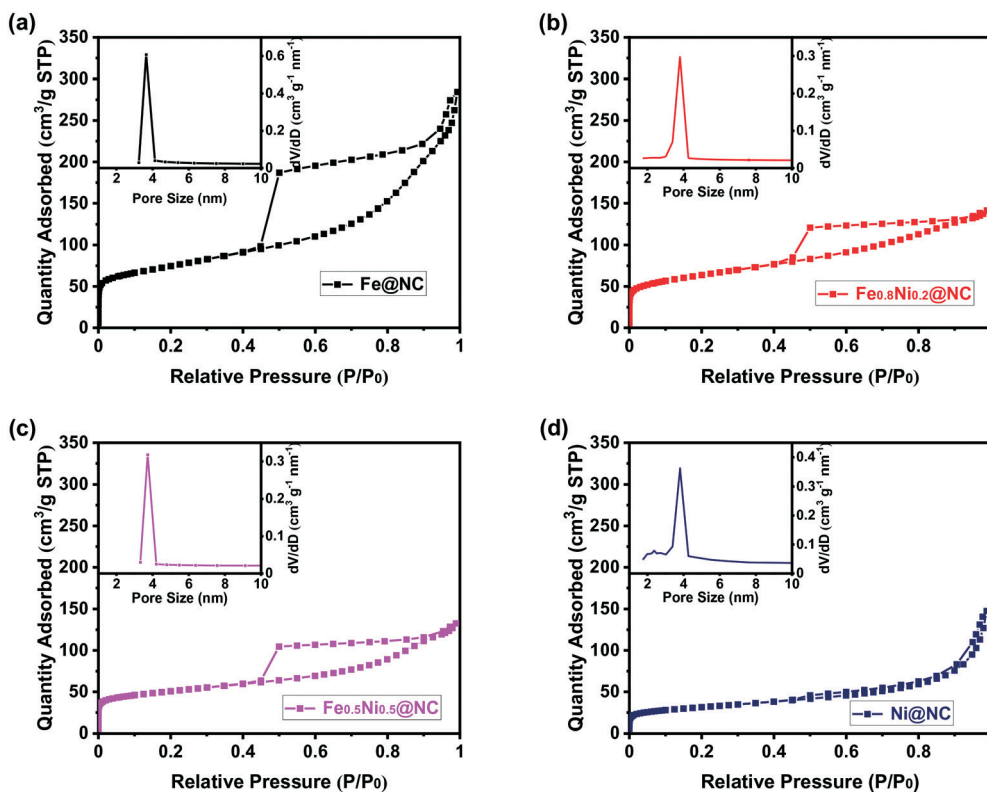**Fig. 4** Nitrogen isothermal desorption curves for (a) Fe@NC, (b) $Fe_{0.8}Ni_{0.2}$@NC, (c) $Fe_{0.5}Ni_{0.5}$@NC, and (d) Ni@NC catalysts. Inset: pore size distribution based on the BJH model.

Table 2 Summary of the texture parameters of the pyrolyzed Fe_xNi_{1-x}@NC catalysts

Samples	$S_{BET}{}^a$ (m² g⁻¹)	$S_{micro}{}^b$ (m² g⁻¹)	$S_{meso}{}^c$ (m² g⁻¹)	$V_{pore}{}^d$ (cm³ g⁻¹)	Pore size (nm)
Fe@NC	250	65	185	0.44	3.6
$Fe_{0.8}Ni_{0.2}$@NC	211	54	157	0.22	3.8
$Fe_{0.5}Ni_{0.5}$@NC	165	59	106	0.21	3.7
Ni@NC	105	25	80	0.23	3.8

^{a} Calculated *via* the BET method. ^{b} Calculated *via* the t-plot method. ^{c} $S_{meso} = S_{BET} - S_{micro}$. ^{d} Calculated based on the N_2 adsorption at $p/p_0 = 0.99$.

and C–N bonds, respectively, which further confirms the presence of N-containing species in the graphene-like carbon matrix.[55] As shown in Fig. S7c,† the N 1s signals for various Fe_xNi_{1-x}@NC catalysts can be deconvoluted into two peaks centered at approximately 398.6 and 401.1 eV, which are assigned to pyridinic N and graphitic N, respectively.[56–58] Additionally, the N 1s signal of pyridinic N in Fe_xNi_{1-x}@NC catalysts exhibits a slightly negative shift with increasing amounts of N. These results suggest that the chemical environment of the N species changes somewhat with the introduction of Ni species, possibly originating from the different coordinative ability between Fe and Ni species, further confirming that a relatively strong interaction could be built between metal NPs and interstitial atoms such as C, O and N that exist in the N-containing carbon materials.

Zeta potential measurements were carried out to study the surface charge properties of the Fe_xNi_{1-x}@NC catalysts. As shown in Fig. 7, the single-metal samples of Fe@NC and Ni@NC possess positive surface charges of +6.1 mV and +1.2 mV, revealing the presence of a weak positive charge on the surface of the catalysts.

The zeta potential of $Fe_{0.9}Ni_{0.1}$@NC and $Fe_{0.8}Ni_{0.2}$@NC increase to +14.0 mV and +18.0 mV, respectively, indicating that additional positive charges are present on the surface of these bimetallic catalysts. Notably, the zeta potential of $Fe_{0.5}Ni_{0.5}$@NC becomes negative (−10.7 mV) when the atomic ratio of Fe/Ni is 0.5/0.5, suggesting that the surface charge of the catalysts may be tuned to a certain extent by changing the composition of the Fe–Ni alloy NPs. Different surface charge properties of Fe_xNi_{1-x}@NC might influence the adsorption/activation capacity for reagents, and thus may lead to different catalytic properties.[59–61]
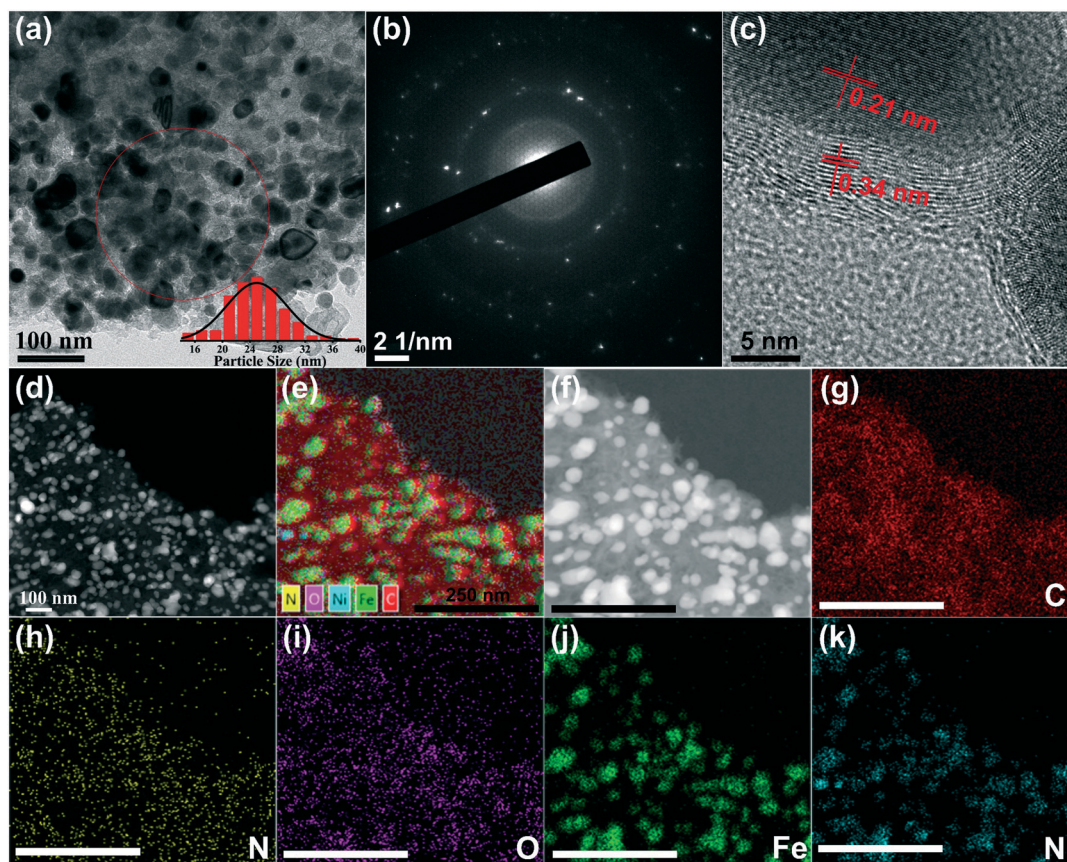
Fig. 5 (a) TEM, (b) SAED pattern, (c) HRTEM, (d) HAADF-STEM images, and (e–k) corresponding elemental mapping results of $Fe_{0.8}Ni_{0.2}@NC$. The inset in (a) shows the statistical analysis of the particle size of $Fe_{0.8}Ni_{0.2}@NC$.
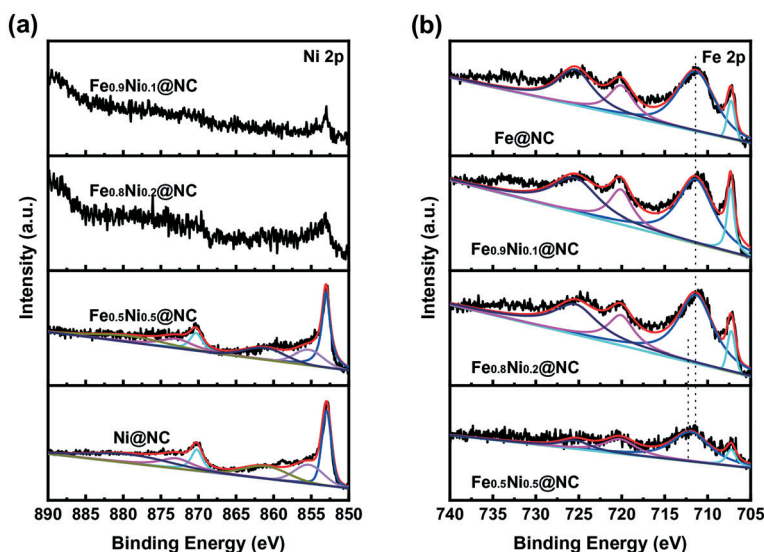

Fig. 6 XPS survey spectra of (a) Ni 2p and (b) Fe 2p for $Fe_xNi_{1-x}@NC$ catalysts.

3.2 Catalytic performance

The catalytic properties of various $Fe_xNi_{1-x}@NC$ catalysts were first investigated for the acylation of *m*-xylene with benzoyl chloride. As given in Table 3, the monometallic Fe@NC catalyst exhibits moderate catalytic activity with 39.5% conversion of benzoyl chloride after 1 h, which is slightly lower than the previous reported result due to the difference in pyrolysis conditions.[31] The catalyst of Ni@NC exhibits relatively low activity for the FCA reaction, and only 3.8% conversion of benzoyl chloride could be achieved after 1 h.

This journal is © The Royal Society of Chemistry 2021

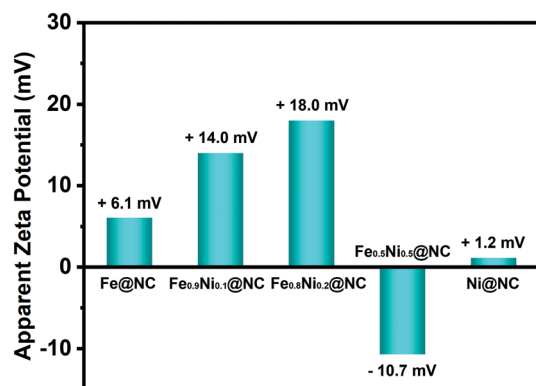*Catal. Sci. Technol.*, 2021, **11**, 7943–7954 | **7949**

Fig. 7 Zeta potential of the Fe_xNi_{1-x}@NC catalysts.

Table 3 Acylation of *m*-xylene with benzoyl chloride over various Fe_xNi_{1-x}@NC catalysts[a]

Entry	Catalysts	Time (h)	Conversion[b] (%)	o/p[c]
1	Blank	5	<1	—
2	Fe@NC	1	39.5	5/95
		5	99.0	4/96
3	$Fe_{0.9}Ni_{0.1}$@NC	1	52.5	4/96
		5	97.6	4/96
4	$Fe_{0.8}Ni_{0.2}$@NC	1	68.7	4/96
		5	98.5	4/96
5	$Fe_{0.5}Ni_{0.5}$@NC	5	<1	—
6	Ni@NC	1	3.8	0/100
		5	41.3	5/95

[a] Reaction conditions: 20 mmol of *m*-xylene, 10 mmol of benzoyl chloride, 10 mmol of dodecane, 0.05 g of catalyst, and temperature = 130 °C. [b] Conversion of benzoyl chloride. [c] *Ortho/para* ratio measured by GC.

Apparently, introducing a certain amount of Ni may significantly increase the catalytic activity of the Fe@NC catalyst. $Fe_{0.8}Ni_{0.2}$@NC exhibited the highest catalytic activity for the acylation, with a 68.7% conversion of benzoyl chloride after 1 h of reaction (Table 3, entry 4). An unexpected result was obtained when using $Fe_{0.5}Ni_{0.5}$@NC as catalyst, and no obvious catalytic activity could be detected after a 5 h reaction. These results suggest that the introduction of a suitable amount of Ni species into Fe-based NP catalysts could create more catalytic active sites for the FCA reactions, while addition of too much Ni species may extinguish the catalytic activity possibly due to the change in the valence electronic structure of the FeNi alloy NPs. Previously, by using DFT calculations, Juan and coauthors demonstrated that the bonding of C to Fe and Ni in $Fe_{0.5}Ni_{0.5}$ alloy with a stacking fault could considerably decrease the Fe–Ni and Ni–Ni bond strengths, thus generating additional inert interface species such as metallic Fe and Ni carbides at the grain boundaries.[54] This might be the main reason why the catalyst of $Fe_{0.5}Ni_{0.5}$@NC is inactive for the FCA reaction.

Fig. 8a shows the time-course tests of various Fe_xNi_{1-x}@NC catalysts, illustrating that the conversion of

benzoyl chloride gradually increases with the extension of reaction time. The recycling experiments reveal that $Fe_{0.8}Ni_{0.2}$@NC catalysts can easily be recycled after simple filtration (without any treatment), and their catalytic activities are well maintained in the four consecutive runs (Fig. 8b). A hot-filtrating experiment demonstrates that no obvious leaching of active Fe species occurs during the reaction term, indicating the high stability of these Fe–Ni bimetallic catalysts (Fig. S8†). Notably, an obvious increase in catalytic activity was detected upon using the spent catalyst for the second run, which indicates that the active sites of the catalyst have been changed somewhat during the course of catalytic reaction.

The catalytic performance of $Fe_{0.8}Ni_{0.2}$@NC was further investigated for the acylation of various aromatic compounds with different groups and other acylation reagents. As shown in Table S2,† entries 1–6, the aromatic compounds with electron-donating ($-CH_3$ and $-OCH_3$) substituents can be easily converted to the corresponding aromatic ketones with relatively high conversion, including some bulky compounds. Benzoylation of mesitylene proceeds more efficiently due to the presence of additional electron donating groups. On the contrary, the acylation of the aromatic compounds with electron-withdrawing ($-F$ and $-NO_3$) substituents was greatly restrained, and no conversion could be achieved over the $Fe_{0.8}Ni_{0.2}$@NC catalyst after reaction for a few hours.

A similar situation was also found for the acylation of anisole with acetic anhydride (Table S2,† entries 7–9). These results suggest that the transformation of aromatic compounds to the corresponding aromatic ketones is highly dependent on the substituents in the aromatic compounds and the types of acylation reagents. Notably, $Fe_{0.8}Ni_{0.2}$@NC was also able to efficiently catalyze the acylation of *m*-xylene with 4-fluorobenzoyl chloride, suggesting that the electron-withdrawing $-F$ group existing in the reactant of acyl chloride had no obvious negative effect on the performance of the catalyst.

To further clarify the nature of the active sites in Fe_xNi_{1-x}@NC catalysts, some additional characterizations such as ICP-AES, XRD, and XPS were carried out to study the spent $Fe_{0.8}Ni_{0.2}$@NC catalyst. As shown in Fig. S9,† the XRD results suggest that the basic structure of the spent $Fe_{0.8}Ni_{0.2}$@NC catalyst remains well after the catalytic tests. In addition, the Fe and Ni contents in the spent catalyst of $Fe_{0.8}Ni_{0.2}$@NC are consistent with that of the fresh one (Table 1), further confirming that the active Fe species are well maintained during the FCA reactions.

The XPS results (Fig. S10 and S11†) revealed that the chemical environment of the main elements in the spent $Fe_{0.8}Ni_{0.2}$@NC catalyst changed somewhat during the acylation process. The Fe 2p spectrum of the spent catalyst can be fitted into five peaks: the two pairs of peaks located at approximately 725.4/711.4 and 713.6/733.1 eV reveal the coexistence of Fe^{3+} and Fe^{2+} species, whereas the other signal at the binding energy of 717.2 eV is ascribed to a satellite peak (Fig. S11a†).[62] The five Ni 2P peaks appearing at
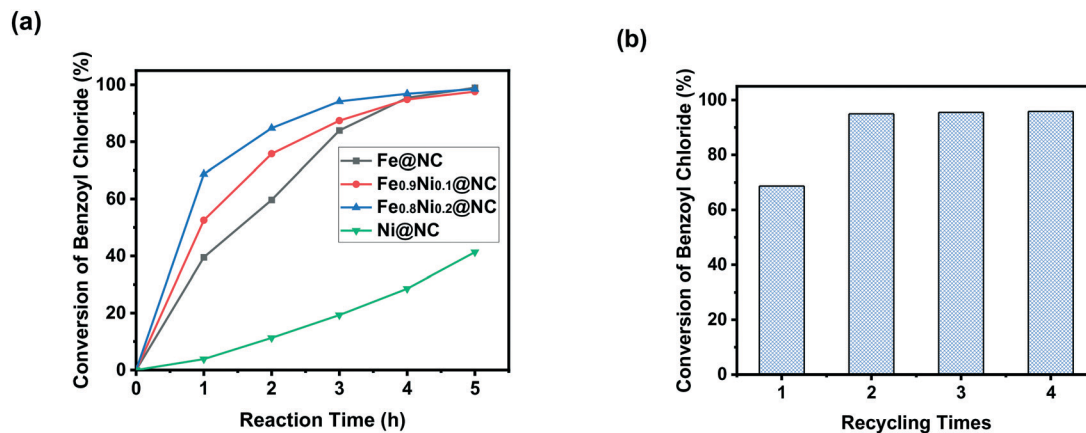
(a)

(b)

Fig. 8 Time-course tests of (a) various Fe_xNi_{1-x}@NC catalysts and (b) recycling experiment for $Fe_{0.8}Ni_{0.2}$@NC (reaction conditions: 20 mmol *m*-xylene, 10 mmol benzoyl chloride, 10 mmol dodecane, 0.05 g of catalyst, and temperature = 130 °C).

approximately 856.4, 862.3, 873.9, 879.1, and 882.6 eV can be assigned to the Ni^{2+} species with different binding environments in the spent $Fe_{0.8}Ni_{0.2}$@NC catalyst, while the signals from the metallic Ni in the fresh catalyst disappeared after the catalytic tests (Fig. S11b†).[24] As shown in Fig. S11c,† obvious Cl $2p_{1/2}$ signals (198.8 eV and 200.3 eV) appeared on the surface of the spent catalyst, indicating the formation of Fe–Cl, Ni–Cl, or C–Cl species through the interaction between the carbon-sphere-encapsulated Fe–Ni NPs with the *in situ*-produced HCl from the acylation reaction.[63–66]

The C 1s spectrum of the spent catalyst shows an extra peak at 288.6 eV, which was assigned to the C═O species possibly originating from the aromatic ketone product (Fig. S11d†).[55] The O 1s spectrum demonstrated that the concentration of M–O species greatly decreased after catalytic reaction (Fig. S11f†), suggesting that a number of M–O species reacted with HCl during the reaction process. These results suggest that additional metal cations (Fe^{3+}, Fe^{2+}, and Ni^{2+}) were formed on the surface of the spent $Fe_{0.8}Ni_{0.2}$@NC catalyst due to the reaction of the metal particles with the *in situ*-produced HCl. In this case, the resultant metal cations acted as new Lewis acid centers to participate in the FCA reactions, thus leading to the spent catalyst exhibiting higher catalytic activity than the fresh one.[31]

Because of the complexity of the bulk structure of catalysts, it is difficult to obtain structural information regarding the area between the inner core and carbon layer by experimental characterization. In order to elucidate where the activity originates, the charge variation of the Fe@NC catalyst before and after the catalytic tests was analyzed. Spin-polarized density functional theory (DFT) was used to calculate the intrinsic electronic properties of catalysts, and the computational details are provided in the experimental section.

XPS characterization showed that some O atoms coordinated with Fe clusters were replaced by Cl atoms after the catalytic tests. Therefore, two simplified models with ion channels (shown in Fig. 9a and b) were constructed to simulate the structure of the fresh and the spent Fe@NC

catalysts. The plots of the contour surface of the charge density difference are shown in Fig. 9c. It can be seen that a small amount of charge was transferred from the outermost layer to the inner, resulting in a weak distribution of positive charge on the surface of the fresh catalyst (top). For the catalysts after the reactions, the substitution of Cl for O dramatically promoted electron transfer and increased the positive charge distribution on the surface (bottom), which more effectively promoted the activation of acyl chloride. We also examined the changes in the zeta potential of catalysts before and after reaction (Fig. S12†). The zeta potentials of the fresh catalysts Fe@NC and $Fe_{0.8}Ni_{0.2}$@NC were +6.1 mV and +18.0 mV, respectively. As for the spent catalysts, the zeta potential dramatically increased to +22.5 mV and +28.5 mV because of the substitution of Cl for O. These results suggest
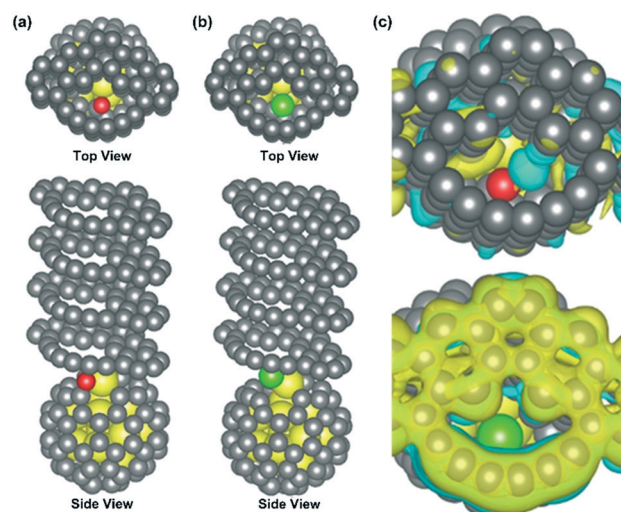

Fig. 9 (a) A simplified model of the fresh Fe@NC catalyst. (b) A simplified model of the spent Fe@NC catalyst after catalytic tests. Grey, red, green, and yellow balls represent carbon, oxygen, chlorine, and iron atoms, respectively. (c) Top view of the charge density differences for the fresh catalysts (top) and the spent catalysts (bottom). Yellow and blue regions represent the distribution of positive and negative charges, respectively.

that the positive charge distribution on the surface of catalysts should play an important role in the activation of acyl chloride, because the larger the positive charge distribution on the surface of catalysts, the more efficient the activation of acyl chloride. Therefore, compared with the fresh catalyst, the spent catalyst (after catalytic tests) exhibited higher catalytic activity.

Based on the above characterization results and the catalytic data, a scheme for describing the structural features of the main active sites of NC-encapsulated Fe-based catalysts (Fe_xNi_{1-x}@NC) and the plausible catalytic mechanism for the FCA reaction are shown in Fig. 10. As mentioned above, a certain amount of metal cations (Fe^{3+} and Ni^{2+}) are present on the surface of the internal FeNi alloy NPs, which should be the main active centers for the Lewis acid-catalyzed FCA reactions. However, the accessibility of metal cations to the reactants (aromatic compounds and acyl chloride) should be rather poor, when considering the fact that all the metal NPs are entirely covered with graphitic carbon layers approximately 5 nm in thickness. In this case, it seems that the external carbon shell may be the location where the catalytic acylation reactions take place.

We suppose that the metal cations (Fe^{3+}, Ni^{2+}) existing on the inner core NPs could exert a positive inductive effect on the outside carbon shell, leading to a partial transfer of positive charge from the inside to the external surface of the spherical particles. Hence, the outside carbon shell can function as a 'chainmail' layer to play a crucial role in transferring positive charge, and to protect the inner metal core from the destructive reaction environments. The so-called 'chainmail catalyst' was firstly reported by Deng *et al.*, who proposed that encapsulating transition metal NPs inside of carbon nanotubes or spheres may become a novel strategy for designing highly durable non-precious metal catalysts to generate the chainmail catalysts that can transfer electrons from the inner core to the external carbon layers, and can also offer effective protection to the metal core from the destruction of the reaction environment.[40,41] In the present case, we believe that the composition-optimized catalyst of $Fe_{0.8}Ni_{0.2}$@NC may also act as a chainmail catalyst that can transfer the inner positive charge to an external surface for catalyzing the FCA reaction, and, at the same time, can

protect the internal active metal sites against destruction by *in situ*-generated HCl.

The relatively high catalytic activity of $Fe_{0.8}Ni_{0.2}$@NC might be at least partially ascribed to the high conductivity of alloyed catalysts, which can lead to a rapid rate of electron transport that is beneficial for improving the catalytic performance of the Fe-based NP catalysts.[24,67] Furthermore, it seems that a portion of the *in situ*-produced HCl can still penetrate the surface carbon shell to react with the inner bimetallic core, and generate additional oxidized metal cations, thus resulting in the formation of additional catalytically active centers to accelerate the FCA reactions. Fortunately, such a reaction does not lead to the loss/leaching of active metal centers during the reaction course, which should also benefit from the effective protection of the graphitic carbon layers. The generation of additional metal cations in the inner core can increase the positive charge of the catalyst, and might induce a greater number of Cl-species to be adsorbed on the external surface of the carbon shell. These changes may positively influence the charge redistribution and further increase the activation capability of the chainmail surface, thus generating a more suitable environment for enhancing the catalytic activity towards FCA reactions.

4. Conclusions

We prepared a series of carbon-based Fe–Ni NP catalysts for Friedel–Crafts acylation reactions through high-temperature pyrolysis of bimetallic metal–organic frameworks. By optimizing the Fe/Ni ratios, a highly active, stable, and eco-friendly catalyst of $Fe_{0.8}Ni_{0.2}$@NC was obtained. The resultant carbon-based composite contains a large number of relatively uniform spherical FeNi alloy NPs encapsulated inside a thin graphitic carbon shell. The DFT calculations and charge density difference reveal the great affinity between the carbon shell and the inner FeNi alloy NPs as a result of charge transfer from the outermost layer to the inner FeNi NPs, thus providing a positive charge distribution on the surface of the catalysts. The external carbon shell of the spherical metal NPs can be activated by the internal metal cations (Fe^{3+} and Ni^{2+}) existing on the surface of inner core, possibly through a positive inductive effect, thus generating catalytically active sites on the external surface of spherical particles for the acylation of aromatic compounds with acyl chlorides. The outside carbon layers then play the role of 'chainmail' that can transfer the internal positive charge to the outside while also providing effective protection to the inside metal NPs from destruction due to reagents such as HCl. This work provides some useful explorations for designing encapsulated alloyed NP catalysts with high activity and stability that hopefully will promote the development of industrial applications for Friedel–Crafts acylation reactions.
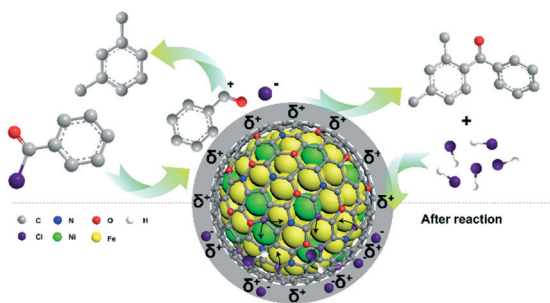

Fig. 10 The structure of the main active sites in the $Fe_{0.8}Ni_{0.2}$@NC catalyst and the plausible catalytic mechanism for the FCA reaction.

7952 | *Catal. Sci. Technol.*, 2021, **11**, 7943–7954

This journal is © The Royal Society of Chemistry 2021

Author contributions

Hao Zhang and Xiaojing Song contributed equally to this work.

Conflicts of interest

There are no conflicts to declare.

Acknowledgements

Notes and references

1 G. Sartori and R. Maggi, *Chem. Rev.*, 2011, **111**, 181–214.

2 J. Liu, Y. Liu, W. Yang, H. Guo, F. Fang and Z. Tang, *J. Mol. Catal. A: Chem.*, 2014, **393**, 1–7.

3 M. Mu, W. Fang, Y. Liu and L. Chen, *Ind. Eng. Chem. Res.*, 2015, **54**, 8893–8899.

4 Z. Fang, W. He, T. Tu, N. Lv, C. Qiu, X. Li, N. Zhu, L. Wan and K. Guo, *Chem. Eng. J.*, 2018, **331**, 443–449.

5 J. Liang, Z. Liang, R. Zou and Y. Zhao, *Adv. Mater.*, 2017, **29**, 1701139–1701159.

6 M. Opanasenko, *Catal. Today*, 2015, **243**, 2–9.

7 M. Bejblová, D. Procházková and J. Čejka, *ChemSusChem*, 2009, **2**, 486–499.

8 M. Shakeri and A. S. Zarnagh, *ChemCatChem*, 2020, **12**, 1–11.

9 Y.-S. Wei, M. Zhang, R. Zou and Q. Xu, *Chem. Rev.*, 2020, **120**, 12089–12174.

10 S.-N. Zhao, X.-Z. Song, S.-Y. Song and H.-J. Zhang, *Coord. Chem. Rev.*, 2017, **337**, 80–96.

11 S. Dang, Q.-L. Zhu and Q. Xu, *Nat. Rev. Mater.*, 2018, **3**, 17075–17088.

12 V. P. Santos, T. A. Wezendonk, J. J. D. Jaén, A. I. Dugulan, M. A. Nasalevich, H.-U. Islam, A. Chojecki, S. Sartipi, X. Sun, A. A. Hakeem, A. C. J. Koeken, M. Ruitenbeek, T. Davidian, G. R. Meima, G. Sankar, F. Kapteijn, M. Makkee and J. Gascon, *Nat. Commun.*, 2015, **6**, 6451–6458.

13 H. Zhang, T. Wang, J. Wang, H. Liu, T. D. Dao, M. Li, G. Liu, X. Meng, K. Chang, L. Shi, T. Nagao and J. Ye, *Adv. Mater.*, 2016, **28**, 3703–3710.

14 L. Jiao, R. Zhang, G. Wan, W. Yang, X. Wan, H. Zhou, J. Shui, S.-H. Yu and H.-L. Jiang, *Nat. Commun.*, 2020, **11**, 2831–2837.

15 Q.-L. Zhu, W. Xia, L.-R. Zheng, R. Zou, Z. Liu and Q. Xu, *ACS Energy Lett.*, 2017, **2**, 504–511.

16 S. Zhao, H. Yin, L. Du, L. He, K. Zhao, L. Chang, G. Yin, H. Zhao, S. Liu and Z. Tang, *ACS Nano*, 2014, **8**, 12660–12668.

17 L. Chen, Y. Zhang, L. Dong, W. Yang, X. Liu, L. Long, C. Liu, S. Dong and J. Jia, *J. Mater. Chem. A*, 2020, **8**, 4369–4375.

18 Y. Xiong, Y. Yang, F. J. DiSalvo and H. D. Abruña, *J. Am. Chem. Soc.*, 2019, **141**, 10744–10750.

19 J.-S. M. Lee, Y.-i. Fujiwara, S. Kitagawa and S. Horike, *Chem. Mater.*, 2019, **31**, 4205–4212.

20 Y.-S. Wei, L. Sun, M. Wang, J. Hong, L. Zou, H. Liu, Y. Wang, M. Zhang, Z. Liu, Y. Li, S. Horike, K. Suenaga and Q. Xu, *Angew. Chem., Int. Ed.*, 2020, **59**, 2–11.

21 Y. Xu, P. Zhai, Y. Deng, J. Xie, X. Liu, S. Wang and D. Ma, *Angew. Chem., Int. Ed.*, 2020, **59**, 21736–21744.

22 C. Wu, X. Zhang, H. Li, Z. Xia, S. Yu, S. Wang and G. Sun, *Chin. J. Catal.*, 2021, **42**, 637–647.

23 J.-C. Li, F. Xiao, H. Zhong, T. Li, M. Xu, L. Ma, M. Cheng, D. Liu, S. Feng, Q. Shi, H.-M. Cheng, C. Liu, D. Du, S. P. Beckman, X. Pan, Y. Lin and M. Shao, *ACS Catal.*, 2019, **9**, 5929–5934.

24 X. Zhao, P. Pachfule, S. Li, J. R. J. Simke, J. Schmidt and A. Thomas, *Angew. Chem., Int. Ed.*, 2018, **57**, 1–7.

25 Z. Wang, M. Li, L. Fan, J. Han and Y. Xiong, *Appl. Surf. Sci.*, 2017, **401**, 89–99.

26 C. Yang, R. Zhao, H. Xiang, J. Wu, W. Zhong, W. Li, Q. Zhang, N. Yang and X. Li, *Adv. Energy Mater.*, 2020, **10**, 2002260–2002269.

27 J. Ma, X. Bai, W. He, S. Wang, L. Li, H. Chen, T. Wang, X. Zhang, Y. Li, L. Zhang, J. Chen, F. Meng and Y. Fu, *Chem. Commun.*, 2019, **55**, 12567–12570.

28 H. L. Huynh, J. Zhu, G. Zhang, Y. Shen, W. M. Tucho, Y. Ding and Z. Yu, *J. Catal.*, 2020, **392**, 266–277.

29 X. Meng, L. Wang, L. Chen, M. Xu, N. Liu, J. Zhang, Y. Yang and M. Wei, *J. Catal.*, 2020, **392**, 69–79.

30 F. Chen, J. Ding, K. Guo, L. Yang, Z. Zhang, Q. Yang, Y. Yang, Z. Bao, Y. He and Q. Ren, *Angew. Chem., Int. Ed.*, 2021, **60**, 2431–2438.

31 H. Zhang, X. Song, D. Hu, W. Zhang and M. Jia, *Catal. Sci. Technol.*, 2019, **9**, 3812–3819.

32 H. Zhang, X. Song, C. Zhao, D. Hu, W. Zhang and M. Jia, *ACS Appl. Nano Mater.*, 2020, **3**, 6664–6674.

33 L. Chen, Y. Zhang, X. Liu, L. Long, S. Wang, W. Yang and J. Jia, *Chem. Commun.*, 2019, **55**, 5651–5654.

34 H. Shang, Z. Jiang, D. Zhou, J. Pei, Y. Wang, J. Dong, X. Zheng, J. Zhang and W. Chen, *Chem. Sci.*, 2020, **11**, 5994–5999.

35 M. Qiao, Y. Wang, Q. Wang, G. Hu, X. Mamat, S. Zhang and S. Wang, *Angew. Chem.*, 2020, **132**, 2710–2716.

36 L. Ye, Y. Ying, D. Sun, Z. Zhang, L. Fei, Z. Wen, J. Qiao and H. Huang, *Angew. Chem., Int. Ed.*, 2020, **59**, 3244–3251.

37 M. Peng, C. Dong, R. Gao, D. Xiao, H. Liu and D. Ma, *ACS Cent. Sci.*, 2021, **7**, 262–273.

38 H. Liu, L. Zhang, N. Wang and D. S. Su, *Angew. Chem., Int. Ed.*, 2014, **53**, 12634–12638.

39 F. Huang, Y. Deng, Y. Chen, X. Cai, M. Peng, Z. Jia, R. Ren, D. Xiao, X. Wen, N. Wang, H. Liu and D. Ma, *J. Am. Chem. Soc.*, 2018, **140**, 13142–13146.

40 L. Yu, D. Deng and X. Bao, *Angew. Chem., Int. Ed.*, 2020, **59**, 15294–15297.

41 D. Deng, L. Yu, X. Chen, G. Wang, L. Jin, X. Pan, J. Deng, G. Sun and X. Bao, *Angew. Chem., Int. Ed.*, 2013, **52**, 371–375.

42 R. V. Jagadeesh, K. Murugesan, A. S. Alshammari, H. Neumann, M.-M. Pohl, J. Radnik and M. Beller, *Science*, 2017, **358**, 326–332.

This journal is © The Royal Society of Chemistry 2021

Catal. Sci. Technol., 2021, **11**, 7943–7954 | **7953**

43 Y. Xu, W. Tu, B. Zhang, S. Yin, Y. Huang, M. Kraft and R. Xu, *Adv. Mater.*, 2017, **29**, 1605957–1605964.

44 G. Kresse and J. Hafner, *Phys. Rev. B: Condens. Matter Mater. Phys.*, 1994, **20**, 14251–14269.

45 P. E. Blöchl, *Phys. Rev. B: Condens. Matter Mater. Phys.*, 1994, **50**, 17953–17979.

46 J. P. Perdew, K. Burke and M. Ernzerhof, *Phys. Rev. Lett.*, 1996, **77**, 3865–3868.

47 S. Grimme, J. Antony, S. Ehrlich and H. Krieg, *J. Chem. Phys.*, 2010, **132**, 154104–154122.

48 L. Feng, S. Yuan, L.-L. Zhang, K. Tan, J.-L. Li, A. Kirchon, L.-M. Liu, P. Zhang, Y. Han, Y. J. Chabal and H.-C. Zhou, *J. Am. Chem. Soc.*, 2018, **140**, 2363–2372.

49 Y. Zhang, X. Hou, X. Li, D. Li, F. Huang and Q. Wei, *J. Colloid Interface Sci.*, 2020, **578**, 805–813.

50 C. Wang, R. Wang, Y. Peng, J. Chen and J. Li, *Chem. Commun.*, 2019, **55**, 10944–10947.

51 D. Nguyen-Trong, K. Pham-Huu and P. Nguyen-Tri, *ACS Omega*, 2019, **4**, 14605–14612.

52 M. Y. Lavrentiev, J. S. Wróbel, D. Nguyen-Manh and S. L. Dudarev, *Phys. Chem. Chem. Phys.*, 2014, **16**, 16049–16059.

53 D. K. Basa, S. Raj, H. C. Padhi, M. Polasik and F. Pawlowski, *Pramana*, 2002, **58**, 783–786.

54 P. Jasen, E. González, G. González, L. Moro and A. Juan, *Phys. Status Solidi B*, 2008, **245**, 2771–2778.

55 X. Han, X. He, L. Sun, X. Han, W. Zhan, J. Xu, X. Wang and J. Chen, *ACS Catal.*, 2018, **8**, 3348–3356.

56 J. Ma, D. Xiao, C. L. Chen, Q. Luo, Y. Yu, J. Zhou, C. Guo, K. Li, J. Ma, L. Zheng and X. Zuo, *J. Power Sources*, 2018, **378**, 491–498.

57 W. Liu, L. Zhang, X. Liu, X. Liu, X. Yang, S. Miao, W. Wang, A. Wang and T. Zhang, *J. Am. Chem. Soc.*, 2017, **139**, 10790–10798.

58 L. Li, C. Tang, Y. Zheng, B. Xia, X. Zhou, H. Xu and S.-Z. Qiao, *Adv. Energy Mater.*, 2020, **10**, 2000789–2000798.

59 W. Zhang, R.-Z. Zhang, Y.-Q. Huang and J.-M. Yang, *Cryst. Growth Des.*, 2018, **18**, 7533–7540.

60 S. K. Alsaiari, S. Patil, M. Alyami, K. O. Alamoudi, F. A. Aleisa, J. S. Merzaban, M. Li and N. M. Khashab, *J. Am. Chem. Soc.*, 2018, **140**, 143–146.

61 Y. Wang, N. Zhang, E. Zhang, Y. Han, Z. Qi, M. B. Ansorge-Schumacher, Y. Ge and C. Wu, *Chem. – Eur. J.*, 2019, **25**, 1716–1721.

62 Y. Zhang, J. Zai, K. He and X. Qian, *Chem. Commun.*, 2018, **54**, 3158–3161.

63 A. C. F. Santos, M. A. MacDonald, A. B. Rocha, N. Appathurai, M. M. Sant'Anna, W. Holetz, R. Wehlitz and L. Zuin, *J. Phys. Chem. A*, 2017, **121**, 4233–4241.

64 Z. Yang, T. Zhao, X. Huang, X. Chu, T. Tang, Y. Ju, Q. Wang, Y. Hou and S. Gao, *Chem. Sci.*, 2017, **8**, 473–481.

65 L. Chen, S. Zuo, Z. Guan, H. Xu, D. Xia and D. Li, *Res. Chem. Intermed.*, 2021, **47**, 795–811.

66 E. Cao, H. Wang, X. Wang, Y. Yang, W. Hao, L. Sun and Y. Zhang, *Sens. Actuators, B*, 2017, **251**, 885–893.

67 T. Zhang, A. G. Walsh, J. Yu and P. Zhang, *Chem. Soc. Rev.*, 2021, **50**, 569–588.

7954 | *Catal. Sci. Technol.*, 2021, **11**, 7943–7954

This journal is © The Royal Society of Chemistry 2021